Evaluation of Signal Degradation Due to Birefringence in a Multiple Reference Optical Coherence Tomography System With Polarization-Based Balanced Detection

Anand Arangath, Kai Neuhaus, *Member, IEEE*, Sergey Alexandrov, and Martin Leahy

***Abstract*— Although time-domain optical coherence tomography (TD-OCT) systems are straightforward to realize, the imaging speed, sensitivity, and imaging depth limit their range of applications. Multiple reference optical coherence tomography (MR-OCT) based on TD-OCT increases imaging range by about tenfold while providing sensitivity to image highly scattering biological samples. The multiple path-delays and free-space construction make MR-OCT also interesting for hybrid and compact systems, filling the gap between fibre-based and wafer-level integrated optical systems. We describe an optical configuration using a balanced detection scheme and the resulting signal properties due to the required use of polarizing optical components. We numerically simulate the signal properties using Jones calculus and compare the results with measurements. We discuss the origin of signal degradation due to birefringence of the sample in OCT and show that the quarter-wave plate in the sample arm of the Michelson interferometer can be adjusted to optimize the signal returning from a birefringent sample thereby improving the visibility of structures of interest. The theory discussed will be useful to understand and minimize signal degradation due to birefringence in Time-Domain and Fourier-Domain OCT systems.**

***Index Terms*—Balanced detection, biophotonics, birefringence, image quality, low cost, multiple reference optical coherence tomography, optical coherence tomography, polarization, optics.**

I. Introduction

OPTICAL coherence tomography (OCT) is a non-invasive imaging technique using low coherent interferometry to produce high-resolution cross-sectional images of subsurface structures in biological tissues and materials [1]. Driven by the commercial availability of miniaturized optics and the need for flexibility in many clinical applications, OCT systems increasingly are designed with reduced form factors and reduced costs while trying to keep imaging performance constant [2], [3]. Most of these miniaturization efforts are focused on spectral-domain OCT (SD-OCT) systems as they offer advantages over time-domain OCT (TD-OCT) in terms of speed and sensitivity [3]–[6]. Time-domain OCT has reduced speed, sensitivity, and axial scan range and may not be of immediate interest for high-end medical grade systems. However, TD-OCT can be more easily adopted for open space optical configurations, such as extreme broad bandwidth light sources. Moreover, TD-OCT can easily be used with off-the-shelf components to make purpose-built systems more readily available compared to other technologies [7]. Portable systems for field usage may have narrower margins to component costs. Reduced scanning speeds and sensitivity may be acceptable for low-cost systems where low data volumes can save costs but are sufficient to obtain relevant information for long-term monitoring and event detection. Multiple-reference OCT (MR-OCT) demonstrates the flexibility of TD-OCT by increasing the axial scan range by simply using a partial mirror [8]. MR-OCT can address applications where system scalability and availability are essential.

Applications of MR-OCT technology in dentistry, dermatology, and non-destructive testing have already been demonstrated [9]–[12]. Unfortunately, the splitting of the reference arm power due to the partial mirror limits the achievable sensitivity of MR-OCT. Therefore, it is essential to compensate as much as possible to achieve sufficient sensitivity for highly scattering samples such as skin. The balanced detection scheme can reduce common-mode noise that originates from the reference and sample arm. Specifically, noise from the light source can efficiently be removed with balanced detection [13], [14]. Neuhaus et al. report a two order of magnitude reduction of excess noise and one order of magnitude reduction of receiver noise compared to single photo-detector mode detection [15]. Balanced detection schemes and the advantages of fibre-based OCT systems are reported in the literature [16]. However, fibre-based systems have limitations regarding miniaturization due to the minimum bending radius of fibre optic guides. Although integrated optical coherence tomography systems on a chip are proposed

Manuscript received 2 July 2022; accepted 5 July 2022. Date of publication 11 July 2022; date of current version 10 August 2022. This work was supported by the European Union's Horizon 2020 Research and Innovation Programme under Grants 761214 and 779960. *(Corresponding author: Martin Leahy.)*

Anand Arangath, Kai Neuhaus, and Sergey Alexandrov are with the Tissue Optics and Microcirculation Imaging Group, Physics School of Natural Sciences, University of Galway, H91 CF50 Galway, Ireland (e-mail: anandarangath@gmail.com; kai.neuhaus@nuigalway.ie; sergey.alexandrov@nuigalway.ie).

Martin Leahy is with the Tissue Optics and Microcirculation Imaging Group, Physics School of Natural Sciences, University of Galway, H91 CF50 Galway, Ireland, and also with the Institute of Photonic Sciences, 08860 Castelldefels, Barcelona, Spain (e-mail: martin.leahy@nuigalway.ie).

Digital Object Identifier 10.1109/JPHOT.2022.3189809

in the literature, their construction may be complex with current technologies. The housing to protect against environmental conditions may increase size and costs, effectively limiting the availability of such systems for the foreseeable future [17]–[19]. Consequently, it seems that free-space time-domain OCT and specifically MR-OCT may still be of interest to fill a gap between larger high-end systems and wafer-level optically integrated systems. Therefore, the MR-OCT method is described using a free-space polarization-based balanced detection configuration to reduce noise and increase sensitivity. Polarization optics for balanced detection can be applied in all OCT configurations. However, it is easier for fibre optic-based systems to use a secondary fibre coupler or circulator to access a second optical channel for balanced detection. Although it may be possible to use the same polarization configuration as for MR-OCT in conjunction with fibre optics, such a configuration would be more complex and introduce losses due to the increased number of fibre couplers. For SD-OCT systems, there is little attraction to looking into a more complex configuration as long as most cameras' saturation power is below the level of power where the excess photon noise exceeds the shot noise. Moreover, a balanced detection raises technical difficulties in balancing not a single point photo-detector, as in TD-OCT and swept-source-based OCT (SS-OCT), but signals delivered by an array of photo-detectors [13].

It is well understood that conventional OCT systems are vulnerable to birefringent artifacts such as extinction banding. Conventional OCT treats the electric field as a scalar quantity and cannot detect the polarization states. When light propagates through the sample being imaged, the polarization states are modified by scattering and birefringence. This can manifest as artifacts in the image. Tissues with stronger birefringence like the sclera in the human eye and highly oriented biological tissues such as cartilage, tendons, burn wounds and muscles cause image artifacts due to polarization effects [20]. Exploratory studies reveal that one in four intensity-based retina images of patients with age-related macular degeneration, glaucoma, or high myopia show artifacts related to polarization [21]. Several techniques have been proposed over time, including polarization-sensitive OCT (PS-OCT), to overcome signal degradation due to polarization mismatch between the sample beam and the reference beam [20], [22]. While PS-OCT systems can generate an additional tissue-specific contrast for advanced diagnosis, they are limited in measurement accuracy by signal to noise ratio [22]. PS-OCT system with balanced detection can be implemented [23], [24]. However, they are complex in construction and expensive [20], [25]. The polarization-based configuration used for MR-OCT requires polarization optics to generate two optical channels with a phase difference of π for balanced detection. The balanced detector generates a single output and cannot retrieve amplitude and phase information of the signal in the two orthogonal polarization axes like in PS-OCT. Because of this, like conventional OCT configurations, polarization-based balanced detection configurations are also known to be susceptible to image artifacts caused by the birefringence of the sample. However, the use of polarization optics opens up the possibility of investigating polarization effects due to the birefringence in the sample. Modelling the signal properties of an MR-OCT system with polarization-based balanced detection, including the effects of the sample birefringence, show that the sample's depth visibility can be improved with the optical components. We confirm the findings from numerical simulation using measurements from a commercial 3 M Scotch Magic tape. A human finger was imaged in-vivo at three different sample arm quarter-wave plate (QWPs) orientations and the visibility of sweat ducts was compared.

II. Theory and Methods

A. Multiple Reference Optical Coherence Tomography

The fundamental theory of MR-OCT can be explained using the theory of TD-OCT [26]–[28]. The time-dependent power P of the interference for TD-OCT is

$$P(t) = P_{\mathrm{r}} + P_{\mathrm{s}} + 2\sqrt{P_{\mathrm{r}}P_{\mathrm{s}}}\mathrm{G}(\delta l)\cos(\omega t + \phi). \tag{1}$$

Where P_r and P_s are the powers in reference and sample arms. δl is the path length difference between the reference and sample arms. If the light source has a Gaussian power distribution then the function $G(\delta l)$ represents the Gaussian envelope of the interference amplitude along δl. The angular frequency is $\omega = 2\pi f$ and ϕ is the initial phase of the frequency content of the interference [15], [28]. Compared to TD-OCT, MR-OCT has an additional partial mirror (PM) in front of the scanning reference mirror. In this study, we used a partial mirror that transmits 20% and reflects 80% of the reference intensity. The SRM was mounted on a custom made voice coil oscillating at 300 Hz with 75 μm scanning range. The multiple reflections between the scanning reference mirror (SRM) and PM enhance the otherwise shallow scanning range of SRM (Fig. 1). The total scanning range or imaging depth (Z_{MRO}) for MR-OCT can be described as

$$Z_{\mathrm{MRO}} = \frac{\delta l}{2}(N+1) + D(N-1) \tag{2}$$

where δl is the scanning range of the SRM, D is the spacing between SRM and PM and N is the number of orders processed. Although infinite reflections and subsequently infinite signal-orders are theoretically available, only up to around twenty orders can be used depending on the sample. The reflectivity, R, of the partial mirror, determines the portion of the reference intensity lost with each reflection. The reference power associated with the N^{th} order reflection is given by

$$P_N = P_{R_0}(1-R)^2 \cdot R^{(N-1)}. \tag{3}$$

The intensity of the incident reference beam is P_{R_0} originating from the beam splitter of the Michelson interferometer. As a consequence of multiple orders of reflections, (1) can be re-written as

$$P_{MRO} = P_{PM_0} + \sum_{N\to\infty} P_r(N) + P_s(N) + 2\sqrt{P_r(N)P_s(N)}\mathrm{G}(\delta l, N)\cos(N\omega t), \tag{4}$$

to incorporate the sum of reference and sample arm powers (P_{r} and P_{s}) for each order N [15]. The component P_{PM_0} is the power

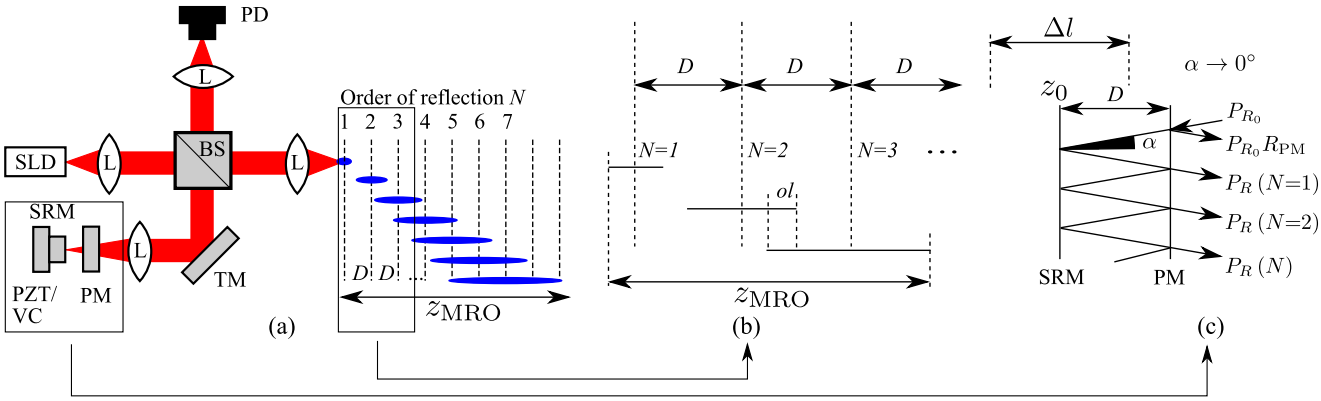

Fig. 1. (a) Schematic of MR-OCT system. SLD: superluminescent diode, L: lens, BS: beam splitter, TM: turning mirror, PM: partial mirror, SRM: scanning reference mirror, PZT/VC: piezo or voice coil actuator, PD: photodetector. (b) The scan range increases with higher orders of reflections (N). This causes the scan ranges of higher orders to for overlapping regions (ol). D is the spacing between SRM and PM. (c) Shows enhanced optical path delays generated by multiple reflections. The angle α is close to zero. δl is the axial scanning range of SRM. The incident wavefront from the beamsplitter with a power P_{R_0} is reflected on the PM with reflectivity R_{PM} generating an optical DC with power $P_{R_0} \cdot R_{PM}$. The beam transmitted through the PM undergoes multiple reflections to give rise to higher-order reference beams with optical powers $P_{R\,(N\,=\,1,\,2,\ldots,\,N)}$.

of the first reflection from the partial mirror back to the beam splitter and the detector describing most of the non-coherent DC background on the detector signal. The Gaussian envelope of N^{th} order can then be described as

$$G(\delta l, N) = \exp\left[-\left(\frac{2\sqrt{\ln 2}N\delta l}{l_c}\right)^2\right]. \tag{5}$$

where l_c is the round trip coherence length of the light source [28], [29].

B. Simulation of Polarization States in an MR-OCT System With Balanced Detection

To realize MR-OCT with balanced detection, a Michelson interferometer that encodes light in the reference and sample arms with polarization states was designed. The returning light from the reference and sample arm are spatially combined at the polarizing beam splitter (PBS).

A detailed schematic of this set-up is demonstrated in Fig. 2. The polarization states in Fig. 2 are representative of ideal alignment conditions with a mirror in the sample arm. The reference arm consists of a quarter-wave plate (QWP_r) with its axis oriented at $45°$ to the incoming linear polarized state. The light reflected by the reference scanning mirror passes through this QWP_r again and returns to the PBS_1 with its linear polarization state rotated by $90°$. Similarly, the QWP_s at $45°$ in the sample arm rotates the incoming polarization state by $90°$ and returns to the PBS_1. The half-wave plate in the detector side (HWP_2) converts the horizontally and vertically polarized beams from the sample and reference arms to diagonally polarized states. A second PBS_2 on the detector arm splits the diagonally polarized beam onto both detectors equally. Consequently, the beams on both detectors will have equal amplitude and interference related oscillations with a phase difference, π, in radians. The noise components including reflections from the partial mirror, auto-correlation due to self-interference within the sample will be in phase. The summing operation at the balanced detector

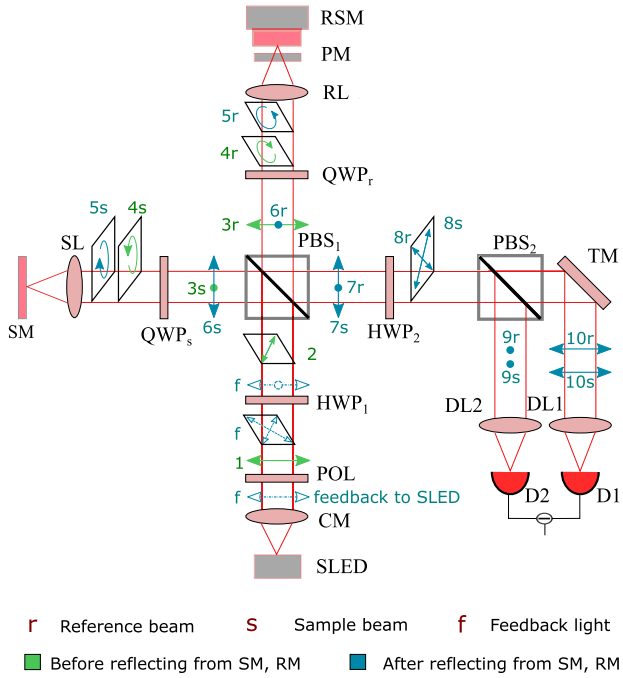

Fig. 2. Schematic of polarization based balanced detection configuration for MR-OCT. The linear polarization states are indicated by arrows and dots. The diagonal and circular polarization states are drawn on a rectangle which represents an X-Y plane perpendicular to the axis of propagation, Z. The dotted arrows represent feedback light towards SLED. The components are SLED: superluminescent diode, CM: collimator lens, POL: polarizer, HWP: Half waveplate, PBS: polarizing beam splitter, QWP: quarter waveplate, GM: galvo mirrors, SL: sample lens, RL: reference lens, PM: partial mirror, RSM: reference scanning mirror, TM: turning mirror, DL1, DL2: detector lenses, D1 and D2 are two sensors of the balanced detector. For this study, we used a commercial balanced detector from Newport Corporation (New focus 2117).

will reject this common noise and thereby improve the overall SNR of the signal. Please note that the reference and sample beams have the same polarization states when they approach the detector.

A numerical simulation was performed to evaluate the polarization states in the MR-OCT system. The goal of the simulation

was to analyse the impact of rotation of reference and sample arm quarter-wave plates on the polarization states of respective beams and their relevance in conjunction with the MR-OCT interference signal. The simulation was first performed with a mirror in the sample arm to evaluate the change of intensity vs the angle of the QWP_s.

The polarization state of light is determined by the direction of the field vector perpendicular to the direction of propagation (z). The polarization state of light can be described by the complex valued field strength along the x (horizontal) and y (vertical) direction, E_x and E_y, respectively. The complex electric field $\mathbf{E}(z,t)$ given by [30]

$$\mathbf{E}(z,t) = \mathbf{E}e^{i(kz-\omega t)} = \begin{pmatrix} E_x \\ E_y \end{pmatrix} e^{i(kz-\omega t)};$$
$$E_x = E_{0x}e^{i\phi_x}, E_y = E_{0y}e^{i\phi_y}. \tag{6}$$

The parameters in (6) are the angular frequency $\omega = 2\pi c/\lambda$, the wave number $k = \omega\tilde{n}/c$, the wavelength λ, velocity of light c, and the complex refractive index $\tilde{n} = n + iK$. To describe the polarization states of light as it passes through the MR-OCT system, the Jones formalism is used [31]. Jones calculus involves representing the electromagnetic field vector $(\mathbf{E})$ as a complex quantity in the 2×1 column matrices (Jones vectors) and the linear optical element in the 2×2 square matrices (Jones matrix). The field $\mathbf{E}$ is the incident field before passing through an optical element represented by a Jones matrix $\mathbf{J}$ and the emerging field with changed polarization states is $\mathbf{E}'$

$$\mathbf{E}' = \begin{bmatrix} E'_x \\ E'_y \end{bmatrix} = \begin{bmatrix} J_{11} & J_{12} \\ J_{21} & J_{22} \end{bmatrix} \cdot \begin{bmatrix} E_x \\ E_y \end{bmatrix} = \mathbf{JE}. \tag{7}$$

The total intensity I of the emerging field is given by

$$I = E_x {E_x}^* + E_y {E_y}^* \tag{8}$$

${E_x}^*$ and ${E_x}^*$ are complex conjugates of E_x and E_y respectively. Carrying out the multiplication after substituting for E_x and E_y from (6) will give

$$I = E_{0x}^2 + E_{0y}^2. \tag{9}$$

The light from the SLED is partially unpolarized and becomes fully polarized after passing through the polarizer POL. The linearly horizontally polarized state for the light after the polarizer is numerically generated directly $(\mathbf{E}_1)$. Since linearly horizontally polarized, the electric field component in the vertical axis is zero $(E_y = 0)$. From (6), the propagator term $(kz - \omega)$ can be neglected since it is not a determining factor for polarization state and $e^{i\phi_x}$ can be neglected since it is uni-modular. It is customary to normalize the total intensity, I of the optical field which results in $E_{0x}^2 = 0$ (see (9)). Therefore, the Jones vector for $\mathbf{E}_1$ can be represented as

$$\mathbf{E}_1 = \begin{bmatrix} E_x \\ E_y \end{bmatrix} = \begin{bmatrix} E_{0x}e^{i\phi_x} \\ E_{0y}e^{i\phi_y} \end{bmatrix} = \begin{bmatrix} 1 \\ 0 \end{bmatrix}. \tag{10}$$

The Jones matrices for an HWP and QWP with the fast axis rotated at an angle θ with the horizontal are given by the following equations [32]

$$\mathbf{J}_{\text{HWP}} = i \begin{bmatrix} \cos 2\theta & \sin 2\theta \\ \sin 2\theta & -\cos 2\theta \end{bmatrix}, \tag{11}$$

$$\mathbf{J}_{\text{QWP}} = i \begin{bmatrix} \frac{1}{\sqrt{2}} + \frac{i}{\sqrt{2}}\cos 2\theta & \frac{i}{\sqrt{2}}\sin 2\theta \\ \frac{i}{\sqrt{2}}\sin 2\theta & \frac{1}{\sqrt{2}} - \frac{i}{\sqrt{2}}\cos 2\theta \end{bmatrix}. \tag{12}$$

To simulate the polarization beam splitter, two separate Jones matrices were used [33], where the matrix for reflection and transmission for an ideal PBS are

$$\mathbf{J}_{\text{PBS}_\text{R}} = \begin{bmatrix} 0 & 0 \\ 0 & 1 \end{bmatrix} \text{ and } \mathbf{J}_{\text{PBS}_\text{T}} = \begin{bmatrix} 1 & 0 \\ 0 & 0 \end{bmatrix}. \tag{13}$$

Throughout the simulation, we assume that the SRM is stationary and the sample mirror is positioned in such a way that optical path length of reference and sample arms are the same. Only values for constructive interference due to superposition are considered. Consequently, (4) and (5) compute only the maximum values of the interference intensity and become dependent only on reference and sample beam intensities. Jones calculus can be applied on Fig. 2 to compute the fields $\mathbf{E}_{8\text{r}}$ and $\mathbf{E}_{8\text{s}}$ with

$$\mathbf{E}_{8\text{r}} = \mathbf{J}_{\text{HWP}_2}(22.5^\circ) \cdot \mathbf{J}_{\text{PBS}_{1,\text{reflection}}} \cdot \mathbf{J}_{\text{QPR}_\text{r}}(-45^\circ) \cdot \mathbf{J}_{\text{mirror}} \cdot \mathbf{J}_{\text{QWP}_\text{r}}(45^\circ) \cdot \mathbf{J}_{\text{PBS}_{1,\text{transmission}}} \cdot \mathbf{J}_{\text{HWP}_1}(22.5^\circ) \cdot \mathbf{E}_1 \tag{14}$$

and

$$\mathbf{E}_{8\text{s}} = \mathbf{J}_{\text{HWP}_2}(22.5^\circ) \cdot \mathbf{J}_{\text{PBS}_{1,\text{transmission}}} \cdot \mathbf{J}_{\text{QPR}_\text{s}}(-45^\circ) \cdot \mathbf{J}_{\text{mirror}} \cdot \mathbf{J}_{\text{QWP}_\text{s}}(45^\circ) \cdot \mathbf{J}_{\text{PBS}_{1,\text{reflection}}} \cdot \mathbf{J}_{\text{HWP}_1}(22.5^\circ) \cdot \mathbf{E}_1. \tag{15}$$

The light beams on detector 1 from the sample and reference arm are

$$\mathbf{E}_{9\text{s}} = \mathbf{J}_{\text{PBS}_{2,\text{reflect}}} \cdot \mathbf{E}_{8\text{s}} \tag{16}$$

$$\mathbf{E}_{9\text{r}} = \mathbf{J}_{\text{PBS}_{2,\text{reflect}}} \cdot \mathbf{E}_{8\text{r}} \tag{17}$$

and detector 2 are

$$\mathbf{E}_{10\text{s}} = \mathbf{J}_{\text{PBS}_{2,\text{transmit}}} \cdot \mathbf{E}_{8\text{s}} \tag{18}$$

$$\mathbf{E}_{10\text{r}} = \mathbf{J}_{\text{PBS}_{2,\text{transmit}}} \cdot \mathbf{E}_{8\text{r}}. \tag{19}$$

The electric field intensities $I_{9\text{s}}, I_{9\text{r}}, I_{10\text{s}}$ and $I_{10\text{r}}$ for $\mathbf{E}_{9\text{s}}, \mathbf{E}_{9\text{r}}, \mathbf{E}_{10\text{s}}$ and $\mathbf{E}_{10\text{r}}$ respectively can be computed using (8). The HWP_2 is aligned at 23.5° so that the amplitudes of electric fields reflected and transmitted by PBS_2 are equal, such that the intensities relation becomes

$$I_{9\text{s}} = I_{10\text{s}} = I_s \tag{20}$$

and

$$I_{9r} = I_{10r} = I_r. \tag{21}$$

To simulate sample arm signal only, we use I_s from (20). For the simplicity of numerical simulation, we assume that the reference mirror is stationary. From (4), when the reference mirror is stationary $(\delta l = 0)$ and there is no interference. The signal on the detector, in this case will be the summation of intensities from sample arm and reference arm.

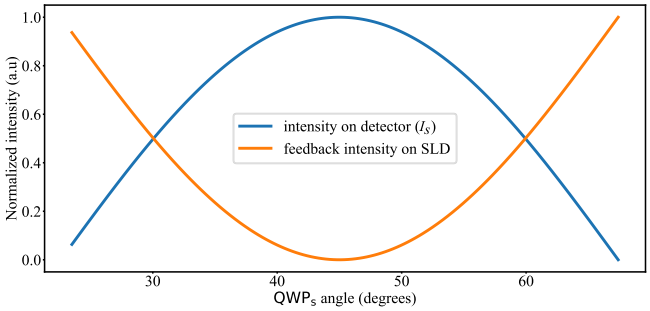

Fig. 3. Simulation of the intensity at the detector with a mirror in the sample arm and different angles of the QWP$_s$. It should be noted that for a single sample mirror only a single order of reflection is available independently of the multiple reference reflections (orders) in the reference arm.

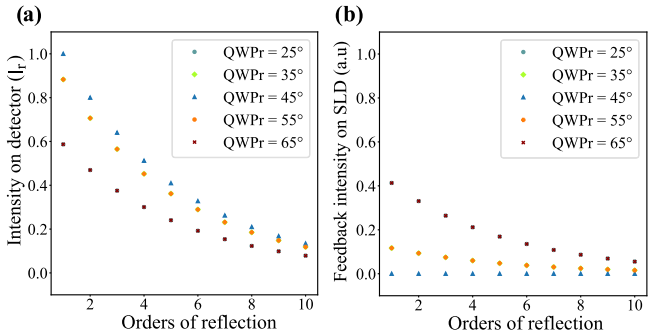

Fig. 4. Simulation of the reference arm powers. Similar to Fig. 3, the powers distributed to the SLED and the detector are shown, but here in two separate plots (detector (a) and SLED (b)). Ten orders of reflections were simulated for five different angles of the QWP$_r$. The maximum power to the detector is at an angle of 45° which also reduces the feedback to the SLED to zero. The roll-off has exponential characteristics for linearly scaled intensities. In the figures, data points overlap for QWP$_r$ = 25°, 65° and for QWP$_r$ = 45°, 55°.

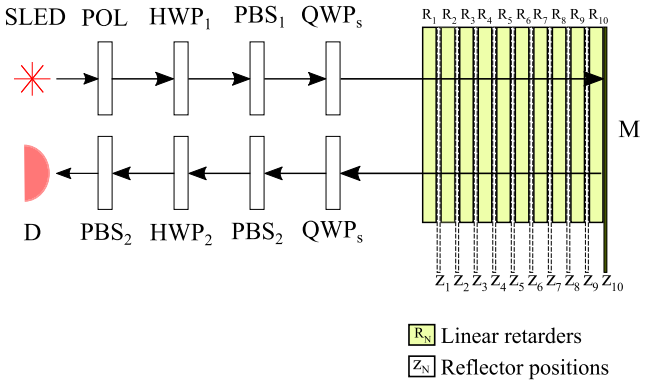

Fig. 5. A simulation model with optical components and birefringent material. The optical components are labelled the same as in Fig. 2. The birefringent material is shown here with ten linear retarders R$_i$ at ten depth positions Z_i and a mirror M. The retarder R is computed with J$_R$ and the mirror M is computed with J$_M$. The model considers here only the sample arm intensity on the detector D.

C. Simulation Using a Mirror on the Sample arm

In the first part of the simulation, we consider the condition in which the sample is a perfectly reflecting mirror. In this case, ideally, the QWP$_s$ will be aligned with its axis oriented at 45° to the incident sample beam in the vertically polarized state ($\mathbf{E}_{3\,s}$). The QWP$_s$ converts the linearly polarized incident beam into circularly polarized light. The reflection on the sample mirror changes the handedness of the circularly polarized state. The second pass through the QWP$_s$ converts the circularly polarized sample beam into the linearly horizontally polarized beam ($\mathbf{E}_{6\,s}$) which is is 100% transmitted by PBS$_1$. However, if the QWP$_s$ axis is rotated either clockwise or anti-clockwise, the beam reflecting from the sample ($\mathbf{E}_{5\,s}$) will be elliptically polarized. Consequently, the sample beam after the second pass through QWP$_s$ will have $\mathbf{E}_x$ and $\mathbf{E}_y$ components mutually oriented at an angle θ. The $\mathbf{E}_x$ component of the field will be transmitted and the $\mathbf{E}_y$ component will be reflected by PBS$_1$. This $\mathbf{E}_y$ component of the sample beam will propagate towards HWP$_1$, POL and finally end up as feedback on the SLED or circulator.

Fig. 3 shows the simulated powers at different angles of the QWP$_s$ for the sample arm intensity towards the detector and the intensity towards the SLED. The interest of the plot is to show that the elliptically polarized light causes feedback and loss of light at the detector. If we lose sample power, it decreases SNR and sensitivity.

In the next step of the simulation, we simulated the reference arm intensity changes on the detector versus the QWP$_r$ axis orientation. To simulate a partial mirror of 80/20 reflection to transmission ratio, the Jones matrix for a mirror with reflectivity 0.8 was used. Multiple reflections can be realized by successive multiplications between the scanning mirror (reflectivity = 1) and the partial mirror. For example, to simulate the second-order reflection, $\mathbf{J}_{\text{mirror}}$ in (14) was replaced by ($\mathbf{J}_{\text{mirror}} \times \mathbf{J}_{\text{partial mirror}} \times \mathbf{J}_{\text{mirror}}$). Fig. 4 shows two separate plots related to the ports of the PBS$_1$ with the fraction propagating towards the detector (Fig. 4(a)) and the feedback towards the SLED (Fig. 4(b)).

If the QWP$_r$ is at 45° relative to the incident polarization states, the light becomes circularly polarized after passing through the QWP$_r$. Reflection on the scanning mirror reverses the handedness of circularly polarized state. All higher orders of reflections involve an odd number of reflections between the PM and SM. This means that every higher-order reference beam in MR-OCT will have the same polarization state and handedness. The light returning after the second pass through QWP$_r$ will be horizontally polarized and completely reflected by PBS$_1$ towards the detector. However, if the QWP$_r$ is rotated either clockwise or anti clockwise, the beam returning to PBS$_1$ will have both E_x and E_y components. The E_x component of the field will be transmitted towards the SLED. The reference beam intensity roll-off obeys eq.3 for all orientations of QWP$_r$. This means that the QWP$_r$ can be used as a reference arm attenuator if the light towards the SLED is blocked using a circulator.

D. Simulation Using a Birefringent Material

Birefringent material is simulated by simplifying the model into several layers with a specified retardance. Fig. 5 shows the

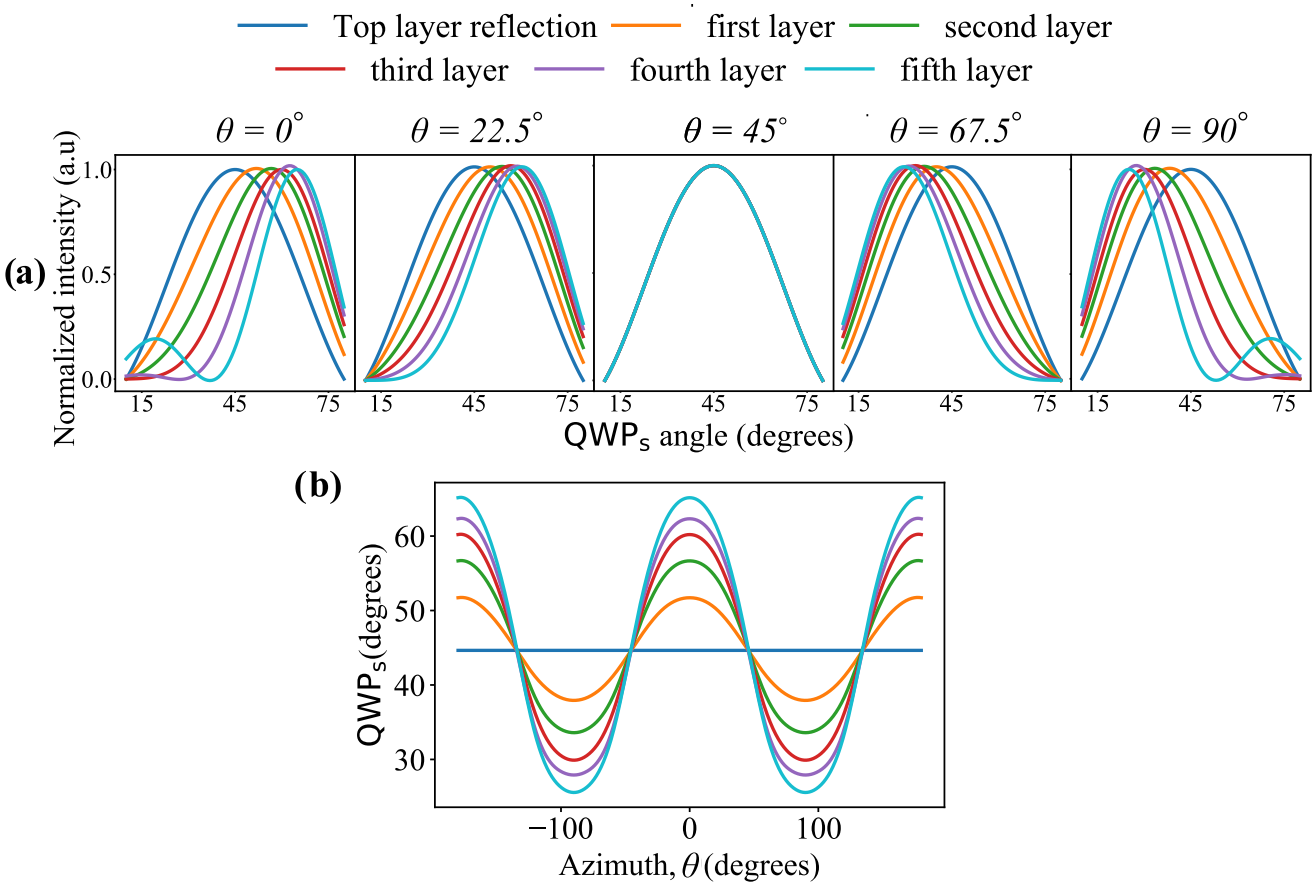

Fig. 6. Shows the results for the layered birefringent sample simulated. (a) Shows the sample arm intensity changes originating from different depth layers versus the $\mathrm{QWP_s}$ orientation for different values of θ, the azimuth. Physically, the azimuth represents different orientations of the optic axis of the sample with respect to the horizontal component of the input polarization state. The sample arm intensity changes for a selected depth versus $\mathrm{QWP_s}$ curve is sinusoidal in shape. The curve for each depth layer is normalized independently. The $\mathrm{QWP_s}$ value corresponding to the peak of the sinusoidal gives maximum intensity for that particular depth. (b) The plot shows the mutual relationship between $\mathrm{QWP_s}$ orientation that gives maximum intensity (the $\mathrm{QWP_s}$ value corresponding to the peak of sinusoidal in Fig. (a) and azimuth. The plot reveals that for the retardance value used for the simulation, $\mathrm{QWP_s}$ has to be rotated either clockwise or anticlockwise from 45° depending on the azimuth or orientation of the sample to improve the visibility of depth layers. The exception is when θ equals to 45° or odd multiples of 45°. In this case, the visibility of all layers will be maximum when $\mathrm{QWP_s} = 45^\circ$ (Also visible from Fig. (a), $\theta = 45^\circ$ where all the sinusoidal curves overlap).

model simulating only the sample arm for ten optical retarders and a reflector. A multi-layer birefringent sample was simulated using 10 linear retarders of the same retardance (R_i). To simplify the simulation, we consider the incidence of a single reflection only. The signal degradation over depth due to multiple scattering and dispersion is not considered. Z_i are possible positions along the depth for the reflector. In other words, reflector position Z_n represents the n^{th} layer of the Scotch tape and there are n layers of linear retarders on top of the reflector. The findings from this modelling are later experimentally confirmed with a multi-layer Scotch tape.

The exact optical properties of Scotch Magic adhesive tape depend on temperature, humidity, tension stress, drawing rate during production, material isotropy, and molecular composition [34]–[42]. Consequently, we expect that the determination of the birefringence of the available Scotch Magic white tape will have considerable variance. Values provided in literature for similar tape or chemical compositions are listed in the Table I. The acronyms for the Materials are for cellulose diacetate (CDA), cellulose triacetate (CTA), cellulose acetate propionate, biaxially oriented polypropylen (PP), ploy vinyl chloride (PVC), polyimide (PI), cellophane (C), cellotape (CT).

The retardance of Scotch tape was determined by Yoo et al. [47] (page 874) and he found for a single tape strip a value of about 0.26 rd (for 500 nm). We used this value to simulate the birefringent sample.

The reflector is simulated using the Jones matrix $\mathrm{J_M}$ for a mirror

$$\mathrm{J_M} = \begin{bmatrix} 1 & 0 \\ 0 & -1 \end{bmatrix}. \tag{22}$$

The linear retarder was simulated using the Jones matrix $\mathrm{J_R}$ for a rotated retarder

$$\mathrm{J_R}(\phi, \theta) = \begin{bmatrix} e^{i\frac{\phi}{2}}\cos^2\theta + e^{-i\frac{\phi}{2}}\sin^2\theta & (e^{i\frac{\phi}{2}} - e^{-i\frac{\phi}{2}})\sin\theta\cos\theta \\ (e^{i\frac{\phi}{2}} - e^{-i\frac{\phi}{2}})\sin\theta\cos\theta & e^{i\frac{\phi}{2}}\sin^2\theta + e^{-i\frac{\phi}{2}}\cos^2\theta \end{bmatrix}. \tag{23}$$

TABLE I
BIREFRINGENCE VALUES FOR DIFFERENT MATERIALS THAT ARE CLOSELY RELATED TO SCOTCH MAGIC TAPE

Material	Birefringence	Birefringence extrapolated
[42] CTA CDA CAP	@750 nm -3×10^{-4} nm 19.5×10^{-4} nm 10.1×10^{-4} nm	@1300 nm -1×10^{-4} nm 20×10^{-4} nm 11×10^{-4} nm
PP [43], [44]	≈ 0.01 (n=1.50@589.3 nm)	N/A
PVC [45]	0.027 (n=1.54)	N/A
PI [24]	0.0263 (n=1.70)	N/A
C [46]	0.0041 (n=1.47@632.8 nm)	N/A
C [34]	0.0077	N/A
C [40]	$\phi = 0.88$@750 nm	$\phi = \frac{2\pi}{\lambda} d\Delta n; d = 40\ \mu\text{m}, \lambda = 750$ nm, $\Delta n = 0.0026$
C [46]	0.0041 $\pm$ 0.0003	N/A
[37] CAP CTA	@750 nm 7.5×10^{-4} -7.5×10^{-4}	@1300 nm 8×10^{-4} -6×10^{-4}
CT [34]	0.0077 $\pm$ 0.0003	N/A
Scotch Magic tape [47]	0.00038@550 nm	N/A

For the rotated retarder in (23) ϕ is the total phase shift between the field components, $\mathrm{E_x}$ and $\mathrm{E_y}$ and θ is the angle of orientation of the fast axis with respect to the X-axis (Azimuth). In general, for elliptical retarders, ϕ takes values between $-\pi/2$ and $\pi/2$.

The same equation can be directly translated to a birefringent sample

$$\phi = \frac{2\pi}{\lambda} d(n_e - n_o) \tag{24}$$

where n_e and n_o are refractive indices along extra-ordinary and ordinary axes and d is the thickness of the sample. The simulation consequently produces as many data points versus depth depending on the number of defined linear retarders. This allows studying the change of the visibility roll-off depending on the azimuth of the sample (θ) and rotation angle of the $\mathrm{QWP_s}$. The intensity changes versus $\mathrm{QWP_s}$ orientation for each layer was separately calculated and plotted in Fig. 6(a). Visibility of each layer is determined by the sample orientation (Azimuth, θ) and $\mathrm{QWP_s}$ orientation.

Ideally, the sample arm intensity changes for selected depth versus $\mathrm{QWP_s}$ rotations would have a sinusoidal characteristic. However, we show only a fraction of the rotation, including the distortions caused by the sample. For each layer, the $\mathrm{QWP_s}$ orientation corresponding to the peak of the sinusoidal (Fig. 6(a)) produces maximum visibility. For a given orientation of sample, the $\mathrm{QWP_s}$ can be adjusted for each layer to optimize the visibility. The beam returning from the birefringent sample will be elliptically polarized. The ellipticity of the returning beam is determined by the cumulative double-pass retardance up to the scatterer or reflector positioned along the depth. This beam will have electric field components in x and y directions. The electric field component in the x direction ($\mathbf{E}_x$) will be transmitted by the $\mathrm{PBS_1}$ towards the detector arm while $\mathbf{E}_y$ will be reflected towards the SLED. The power lost due to the light reflected by the $\mathrm{PBS_1}$ towards the SLED causes degradation of signal in the interferometer as it does not reach the detector. By adjusting the orientation of $\mathrm{QWP_s}$ with the incident polarization state, the proportion of x and y components present in the returning beam can be altered. The $\mathrm{QWP_s}$ orientation can be adjusted for a selected ellipticity in such a way that the $\mathbf{E}_x$ component is maximum after passing through $\mathrm{QWP_s}$ in the returning path. In this case, the intensity of light returning from selected depths can be maximized. The disadvantage is that the visibility of certain other depth regions may be compromised. From Fig. 6, it is evident that the sample arm intensities on detector returning from reflectors at different depths are heterogeneously influenced by the $\mathrm{QWP_s}$ orientation and the azimuth of the sample. Therefore, it is of interest to evaluate the dependency of intensity roll-off in a birefringent sample for different orientations of $\mathrm{QWP_s}$ and azimuths.

Sample arm intensity roll-off and roll-off of total signal (sample arm + reference arm) are separately plotted in Fig. 7(a) and Fig. 7(b) respectively. The sample arm intensity roll-off in Fig. 7(a) is determined exclusively by the value of retardation used to simulate the linear retarders in Fig. 5. The intensity roll-off in Fig. 7(a) is determined by the combination of sample arm roll-off and reference arm roll-off (Fig. 4(a)). Here, according to (3), the intensity contribution from the reference arm will be different for signals representing different depth layers in the sample. Please note that the attenuation of light in the medium due to scattering, optical effects such as depolarization, diattenuation are not accounted for here. The roll-off models simulated reveals that depending on θ and ϕ, the orientation of $\mathrm{QWP_s}$ can be optimized to improve the visibility for depth ranges of interest. To verify this, a white Scotch tape was imaged at different azimuths and $\mathrm{QWP_s}$ orientations.

III. EXPERIMENTAL RESULTS AND DISCUSSIONS

To verify the results from the simulation, a the sample was constructed by slicing off 15 layers from a commercial 3 M Scotch Magic tape and then stacking them on a coverslip. Scotch tape was selected because it shows moderate linear retardance that can be used to control and investigate polarization properties, is easy to obtain, and it is a material with good light scattering properties. The linear birefringence of a single Scotch tape film is approximately oriented along the strip axis [47]. The sample was fixed on a rotation mount from Thorlabs, Inc.(Fig. 8(c)). The rotation mount allowed to image the sample at different azimuths (θ). To recreate the results in Fig. 8, the sample was imaged at different azimuths and $\mathrm{QWP_s}$ orientations.

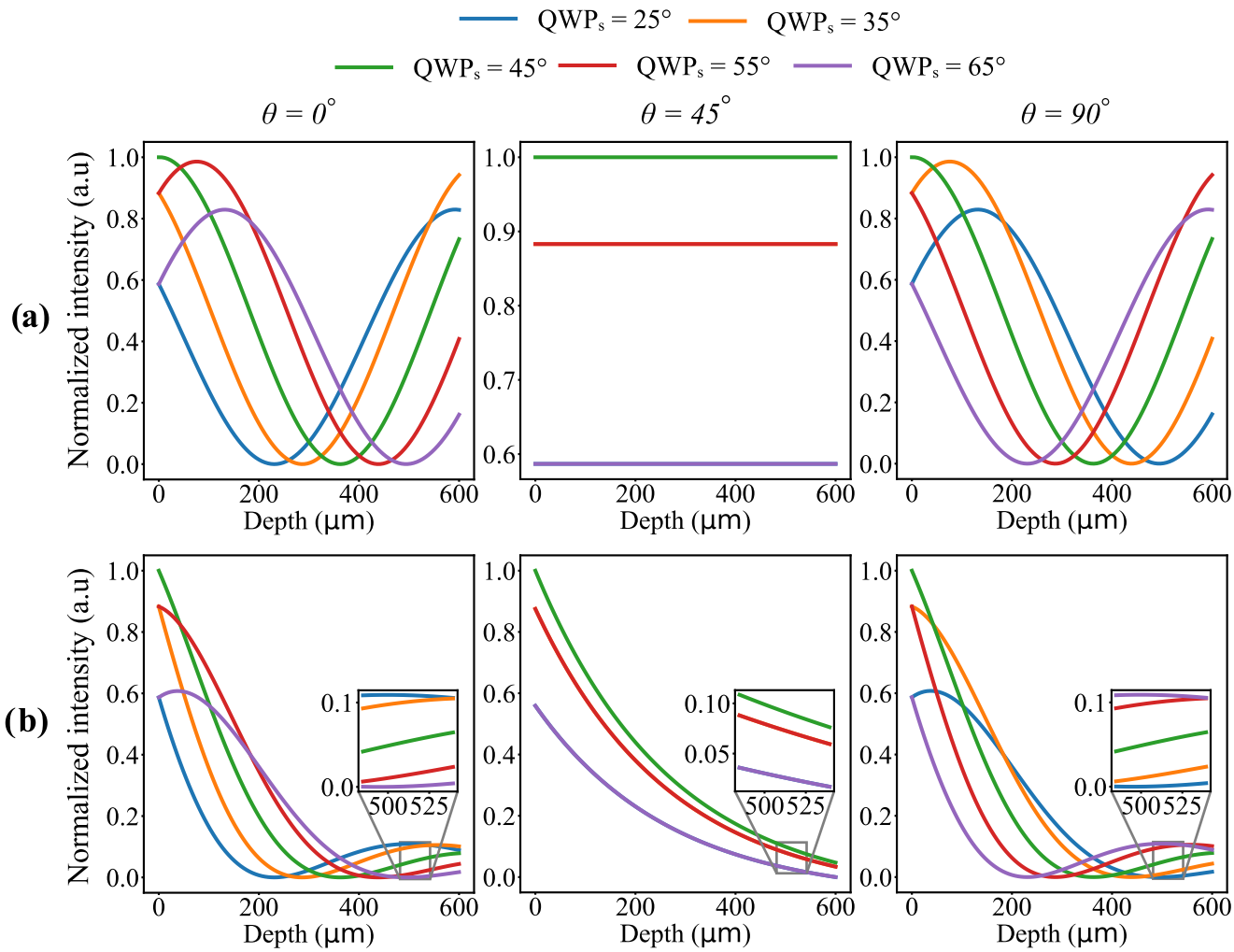

Fig. 7. The plots show how the intensity roll-off of a birefringent sample depends on the QWP$_s$ orientation and θ, azimuth of the sample. Three values that exhibit extreme intensity variations versus QWP$_s$ orientations were selected for θ ($0°, 45°$and $90°$) based on Fig. 6(b). (a) The first row of images represent the sample arm intensity roll-off at the detector versus depth. It can be seen that depending on θ, the roll-off characteristics are different for different orientations of QWP$_s$. When $\theta = 45°$, the sample arm intensity roll-off due to birefringence is a flat line indicating independence of roll-off from polarization effects. (b) Shows the roll-off of total interference intensity (reference arm + sample arm) from the simulated birefringent sample at the detector. For these plots, the reference arm intensity roll-off due to higher orders of MR-OCT (Fig. 4(a)) is incorporated. From the plots, it can be observed that when $\theta = 0°$, the intensity at deeper regions (400 μm to 600 μm) can be improved by orienting the QWP$_s$ at $25°$. On the other hand, when $\theta = 90°$, QWP$_s$ $= 65°$ gives the best visibility at 400 μm to 600 μm depth region. When $\theta = 45°$, the intensity is maximum at all depths when QWP$_S$ $= 45°$. Also, the roll-off curves for complementary QWP$_s$ orientations overlap.

The intensity changes for selected layers were plotted against QWP$_s$ orientations as shown in Fig. 8(a).

The data in Fig. 8(a) was obtained by plotting the intensity changes versus QWP$_s$ orientations for selected layers at selected sample orientations (θ). The data points were generated by taking the mean intensity at selected depth positions from all the 500 available A-lines. The standard error in this mean calculation is represented by the error bars. The model in Fig. 6(a) was fitted over the data points to obtain the sinusoidal curves. The value of θ was not predetermined. The orientation of the sample where the intensity versus QWP$_s$ orientation plots for all the layers overlapped was selected as $\theta = 45°$. Fig. 8(b) was generated by plotting the QWP$_s$ orientation corresponding to the peak of sinusoidal for each layer against θ. Only a range of θ was selected ($0°$ to $90°$) to reasonably limit the data acquisition process. On the data points thus generated, a sinusoidal fitting was applied. To evaluate the dependency of intensity roll-off in the Scotch tape sample for different orientations of QWP$_s$ and azimuths, averaged A-lines from conventional OCT images were analyzed. The averaged A-lines in this case directly gives the intensity roll-off versus depth and allow the visibility of each layer to be calculated.

The plots in fig. 9 evaluate how the intensity roll-off of Scotch tape sample depends on the QWP$_s$ orientation and θ, azimuth of the sample. It can be observed from the grayscale images in Fig. 9(a) that when $\theta = 0°$, deeper layers become more visible as we rotate the QWP$_s$ from $25°$ to $65°$. When $\theta = 90°$, deeper layers have higher intensity when the QWP$_s$ orientations tend towards $25°$. When $\theta = 45°$, all layers are most visible at QWP$_s$ $= 45°$. For better visualization of the intensity roll-off of

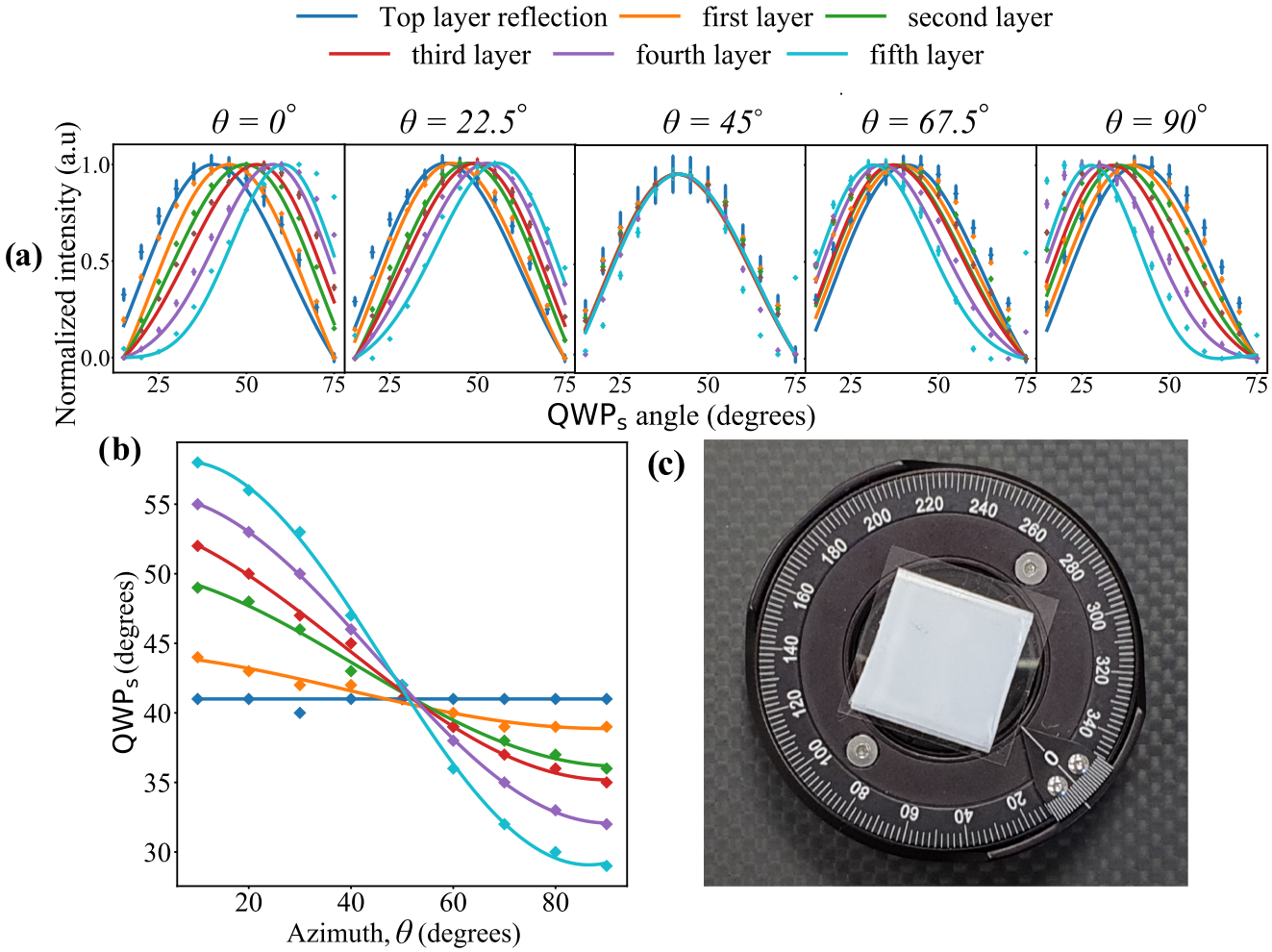

Fig. 8. Shows the experimental results from the birefringent sample imaged. (a) Shows the intensity changes originating from different layers of Scotch tape versus the QWP_s orientation for different values of θ, the azimuth. Physically, the azimuth represents different orientations of the optic axis of the sample with respect to the horizontal component of the input polarization state. The intensity changes for selected layers versus QWP_s curve is sinusoidal in shape as expected from Fig. 6(a). The sinusoidal curve for each depth layer is normalized independently. The QWP_s value corresponding to the peak of the sinusoidal gives maximum intensity for that particular layer. (b) The plot recreates the results from Fig. 6(b) to show the mutual relationship between QWP_s orientation that gives maximum intensity (the QWP_s value corresponding to the peak of sinusoidal in Fig. (a) and azimuth. (c) Shows photograph from the sample used. 15 layers sliced off from a Scotch tape were stuck together on a cover slip. The cover slip was then mounted on a rotating mount to image the samples at different azimuths.

depth layers, the mean A-line (averaged from all the 500 A-lines) for different θ and QWP_s orientations were plotted in Fig. 9(b). It can be observed from the enlarged images near 500 μm depth that the intensity is maximum at $QWP_s = 65°, 45°$ and $25°$ for $\theta = 0°, 45°$ and $90°$ respectively. This is in correlation with the prediction from the plots in fig.7(b). The model also predicted the overlap of intensity roll-off curves from complementary angles of QWP_s while $\theta = 45°$. This can be verified from the experimental results provided in Fig. 9(b) ($\theta = 45°$).

To quantitatively evaluate the changes in visibility of layers with QWP_s orientations, the Michelson contrast was used. The Michelson contrast describes the visibility of periodic intensity changes based on the minimum (I_{min}) and maximum (I_{max}) amplitude [48]. To quantify the visibility of the tape layers, we fitted a sinusoidal function over the intensity undulations originating from the axial intensity variations. We then used the Michelson contrast equation $(I_{min} - I_{max})/(I_{min} + I_{max})$ to obtain a value for visibility for further comparison. The underlying fitting model was a sum of a sinusoidal and an exponential function. The exponential function accommodates the continuous absolute intensity roll-off vs depth. The sinusoidal model follows the intensity undulations of the tape layers (Fig. 9(b)) and then measures the tape layer visibility based on the contrast (Fig. 9(c)). Depending on the azimuth of the sample, the Michelson contrast for the tape layers changes and can be adjusted with the QWP_s. Adjusting the QWP_s allows to adapt to the birefringence of samples and improve the visibility of regions of interest. To demonstrate the potential of imaging with different QWP_s orientations to improve the visibility of relevant structures within biological tissues, a human finger was imaged in-vivo at three different QWP_s orientations and the visibilities of sweat ducts were compared (Fig. 10). The tissue in the finger is birefringent due to the presence of narrow fibrous structures. To compare the visibility, contrast to noise

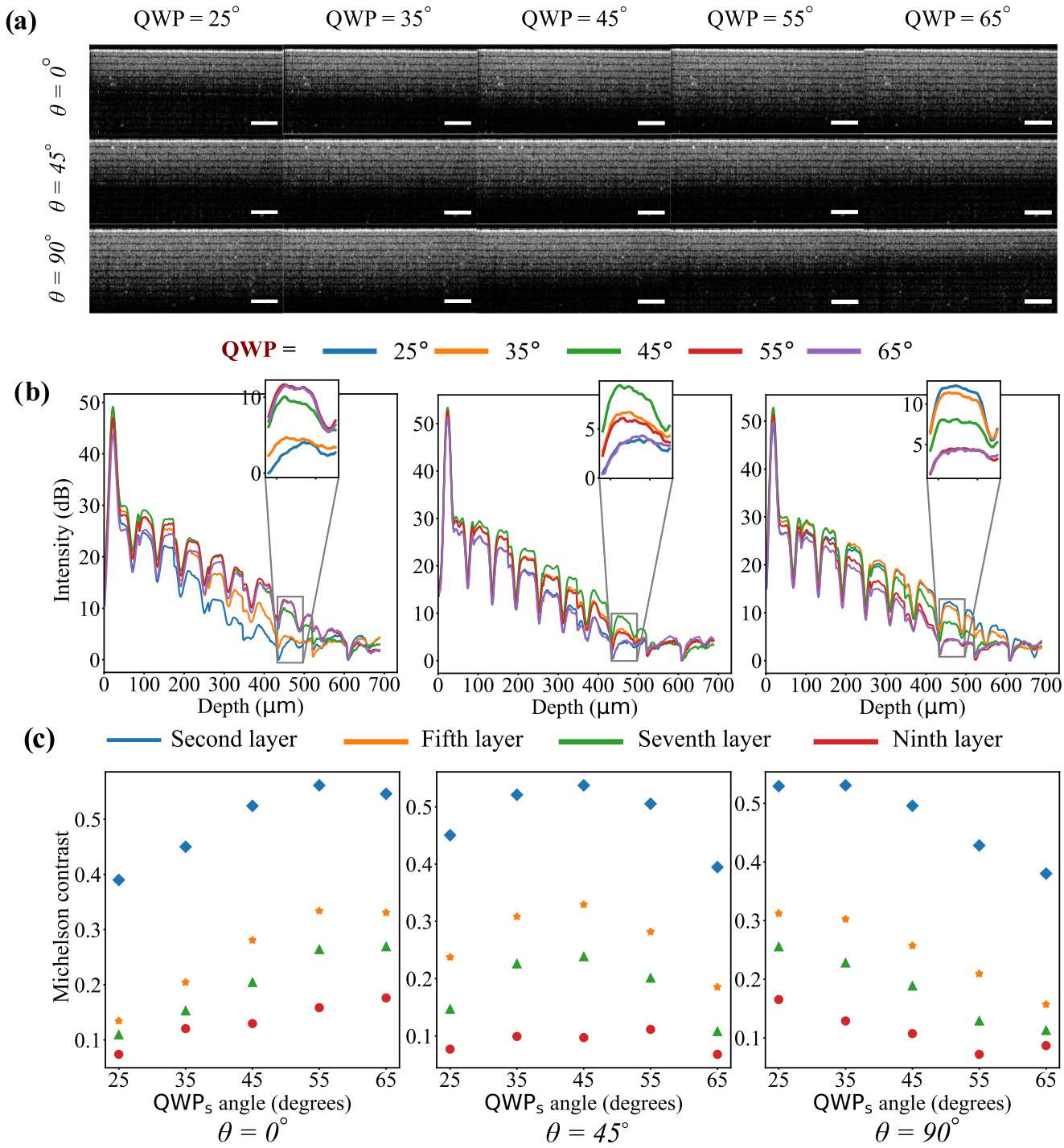

Fig. 9. The plots evaluate how the intensity roll-off of Scotch tape sample depends on the QWP_s orientation and θ, azimuth of the sample. Three values that exhibit extreme intensity variations versus QWP_s orientations were selected for θ (0°, 45°and 90°) based on Fig. 6(b). (a) Shows conventional grayscale images (logarithmic scale) from different azimuths of the sample acquired with different QWP_s orientations. The scale bar represents 225 μm. (b) Shows the averaged A-lines from intensity-based OCT images. The averaged A-lines can be used to evaluate the dependency of θ and QWP_s on intensity roll-off. (c) Shows how the Michelson contrast for specified layers varies against QWP_s orientations.

ratio (CNR) for structures in the yellow and orange insets were calculated using $|S_A - S_B|/\sigma$ where S_A and S_B are signal intensities for signal producing structures A (sweat duct within inset) and B (median background intensity in the selected region) respectively and σ is the standard deviation of the image noise. The CNR values obtained are listed in the Table II. It can be seen that the visibility of sweat ducts improved when imaged with $QWP_s = 65°$ compared to $QWP_s = 25°$ and 45°.

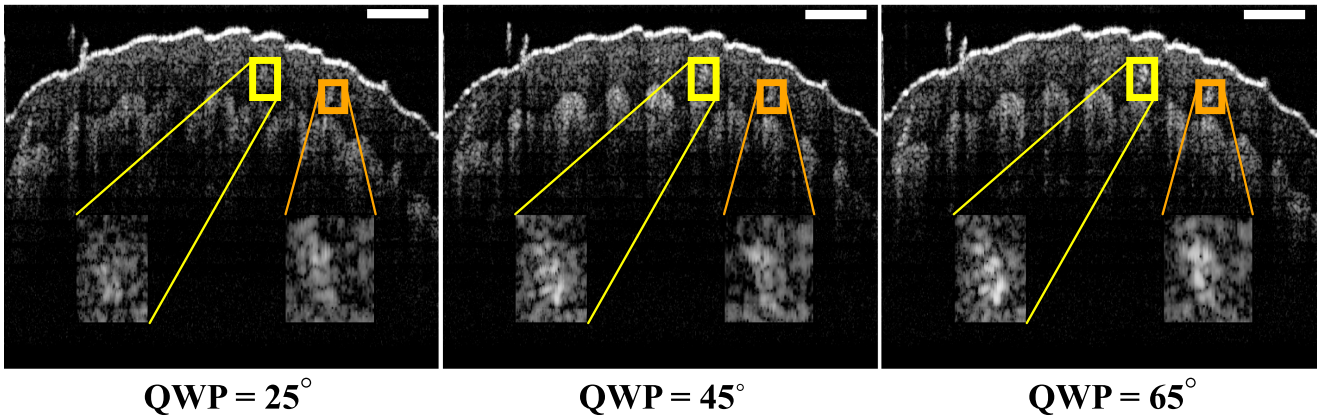

Fig. 10. Shows the changes in visibility of sweat ducts when a finger was imaged with three different orientations of $\mathrm{QWP_s}(25°, 45°$ and $65°$ from left to right). A quantitative comparison of visibility of structures within the insets is provided in the Table II. The scalebar represents 200 µm. The images were acquired in vivo from one of the author's fingertip using the MR-OCT system with polarization-based balanced detection.

TABLE II
LIST OF THE CNR VALUES CALCULATED TO EVALUATE THE VISIBILITY OF SWEAT DUCTS UNDER DIFFERENT $\mathrm{QWP_s}$ ORIENTATIONS. STRUCTURE A IS THE SWEAT DUCT MARKED BY THE YELLOW INSETS. B REFERS TO THE SWEAT DUCT IN ORANGE INSETS. IT WAS OBSERVED THAT THE VISIBILITY OF THESE STRUCTURES IMPROVED WHEN IMAGED WITH $\mathrm{QWP_s} = 65°$

$\mathrm{QWP_s}$	CNR (A)	CNR (B)
$25°$	1.7	1.8
$45°$	2.2 (29% improvement over $\mathrm{QWP_s} = 25°$)	1.9 (6% improvement over $\mathrm{QWP_s} = 25°$)
$65°$	2.5 (13% improvement over $\mathrm{QWP_s} = 45°$ and 47% improvement over $\mathrm{QWP_s} = 25°$)	2.0 (5% improvement over $\mathrm{QWP_s} = 45°$ and 11% improvement over $\mathrm{QWP_s} = 25°$)

IV. CONCLUSION

We described an MR-OCT with a polarization-based balanced detection configuration and numerically evaluated the resulting signal properties in relation to the polarization optics used and the birefringence of the sample imaged. The numerical simulation can accurately model the image contrast changes caused by the birefringence of the sample. We demonstrated in a human finger that imaging with different orientations of the quarter-wave plates in the sample arm could influence the visibility of structures. Using Scotch tape as a simple layered model, we showed that the visibility of deeper regions in a birefringent sample could be improved. This enhanced imaging range is particularly interesting for low-cost systems with constrained imaging range due to moderate sensitivity when imaging materials and biological tissues with strong birefringence like the sclera in the human eye, cartilage, tendons, burn wounds and muscles. The theory and results discussed in the manuscript can be translated to other OCT systems such as FD-OCT and TD-OCT. Even if the system is not equipped with polarization components such as a quarter-wave plate in the sample arm, imaging the birefringent samples at different azimuths can influence the visibility of structures. Under constrained imaging conditions where rotating the sample is not practical, an optical configu- ration such as the one described in this study can be useful.

ACKNOWLEDGMENT

The authors also acknowledge the University of Galway for facilities and funding. The materials presented and views expressed here are the responsibility of the authors only. The EU Commission takes no responsibility for any use made of the information set out.

REFERENCES

[1] D. Huang et al., "Optical coherence tomography," *Science*, vol. 254, no. 5035, pp. 1178–1181, Nov. 1991.
[2] G. L. Monroy, J. Won, D. R. Spillman, R. Dsouza, and S. A. Boppart, "Clinical translation of handheld optical coherence tomography: Practical considerations and recent advancements," *J. Biomed. Opt.*, vol. 22, no. 12, Dec. 2017, Art. no. 121715.
[3] G. Song et al., "First clinical application of low-cost OCT," *Transl. Vis. Sci. Technol.*, vol. 8, no. 3, May 2019, Art. no. 61.
[4] A. F. Fercher, C. K. Hitzenberger, G. Kamp, and S. Y. El-Zaiat, "Measurement of intraocular distances by backscattering spectral interferometry," *Opt. Commun.*, vol. 117, no. 1, pp. 43–48, May 1995.
[5] B. Golubovic, B. E. Bouma, G. J. Tearney, and J. G. Fujimoto, "Optical frequency-domain reflectometry using rapid wavelength tuning of a Cr^4++: Forsterite laser," *Opt. Lett.*, vol. 22, no. 22, pp. 1704–1706, Nov. 1997.
[6] M. A. Choma, M. V. Sarunic, C. Yang, and J. A. Izatt, "Sensitivity advantage of swept source and Fourier domain optical coherence tomography," *Opt. Exp.*, vol. 11, no. 18, pp. 2183–2189, Sep. 2003.
[7] P. M. McNamara et al., "Development of a first-generation miniature multiple reference optical coherence tomography imaging device," *J. Biomed. Opt.*, vol. 21, no. 12, Dec. 2016, Art. no. 126020.
[8] M. Leahy, J. Hogan, C. Wilson, H. Subhash, and R. Dsouza, "Multiple reference optical coherence tomography (MR-OCT) system," in *Proc. SPIE Dyn. Fluctuations Biomed. Photon. X*, 2013, vol. 8580, Art. no. 85800L.

[9] R. Dsouza, H. Subhash, K. Neuhaus, J. Hogan, C. Wilson, and M. Leahy, "Dermascope guided multiple reference optical coherence tomography," *Biomed. Opt. Exp.*, vol. 5, no. 9, pp. 2870–2882, Sep. 2014.

[10] R. Dsouza, H. M. Subhash, K. Neuhaus, J. Hogan, C. Wilson, and M. Leahy, "3D nondestructive testing system with an affordable multiple reference optical-delay-based optical coherence tomography," *Appl. Opt.*, vol. 54, no. 18, pp. 5634–5638, Jun. 2015.

[11] R. Dsouza et al., "Assessment of curing behavior of light-activated dental composites using intensity correlation based multiple reference optical coherence tomography," *Lasers Surg. Med.*, vol. 48, no. 1, pp. 77–82, Jan. 2016.

[12] K. Neuhaus et al., "Simultaneous en-face imaging of multiple layers with multiple reference optical coherence tomography," *J. Biomed. Opt.*, vol. 22, no. 8, Aug. 2017, Art. no. 086006.

[13] A. G. Podoleanu, "Unbalanced versus balanced operation in an optical coherence tomography system," *Appl. Opt.*, vol. 39, no. 1, pp. 173–182, Jan. 2000.

[14] G. Abbas, V. Chan, and T. Yee, "A dual-detector optical heterodyne receiver for local oscillator noise suppression," *J. Lightw. Technol.*, vol. 3, no. 5, pp. 1110–1122, Oct. 1985.

[15] K. Neuhaus et al., "Performance review of multiple reference versus time domain optical coherence tomography," *IEEE Photon. J.*, vol. 10, no. 3, Jun. 2018, Art. no. 3400214.

[16] A. M. Rollins and J. A. Izatt, "Optimal interferometer designs for optical coherence tomography," *Opt. Lett.*, vol. 24, no. 21, pp. 1484–1486, Nov. 1999.

[17] B. D. Goldberg, S. M. R. M. Nezam, P. Jillella, B. E. Bouma, and G. J. Tearney, "Miniature swept source for point of care optical frequency domain imaging," *Opt. Exp.*, vol. 17, no. 5, pp. 3619–3629, Mar. 2009.

[18] S. Schneider, M. Lauermann, P.-I. Dietrich, C. Weimann, W. Freude, and C. Koos, "Optical coherence tomography system mass-producible on a silicon photonic chip," *Opt. Exp.*, vol. 24, no. 2, pp. 1573–1586, Jan. 2016.

[19] B. I. Akca et al., "Miniature spectrometer and beam splitter for an optical coherence tomography on a silicon chip," *Opt. Exp.*, vol. 21, no. 14, pp. 16648–16656, Jul. 2013.

[20] Y. Yang, L. Wu, Y. Feng, and R. K. Wang, "Observations of birefringence in tissues from optic-fibre-based optical coherence tomography," *Meas. Sci. Technol.*, vol. 14, no. 1, pp. 41–46, Jan. 2003.

[21] T. Minami et al., "Conventional OCT artifacts in the human sclera revealed by polarization-sensitive OCT," *Invest. Ophthalmol. Vis. Sci.*, vol. 60, no. 9, pp. 1591–1591, Jul. 2019.

[22] M. J. Everett, K. Schoenenberger, B. W. Colston, and L. B. D. Silva, "Birefringence characterization of biological tissue by use of optical coherence tomography," *Opt. Lett.*, vol. 23, no. 3, pp. 228–230, Feb. 1998.

[23] H. Pahlevaninezhad, A. M. D. Lee, L. Cahill, S. Lam, C. MacAulay, and P. Lane, "Fiber-based polarization diversity detection for polarization-sensitive optical coherence tomography," *Photonics*, vol. 1, no. 4, pp. 283–295, Dec. 2014.

[24] M.-C. Oh, M.-H. Lee, and H.-J. Lee, "Polymeric waveguide polarization splitter with a buried birefringent polymer," *IEEE Photon. Technol. Lett.*, vol. 11, no. 9, pp. 1144—1146, Sep. 1999.

[25] N. Wang, X. Liu, Q. Xiong, J. Xie, S. Chen, and L. Liu, "Polarization management to mitigate misalignment-induced fringe fading in fiber-based optical coherence tomography," *Opt. Lett.*, vol. 42, no. 15, pp. 2996–2999, Aug. 2017.

[26] A. F. Fercher, "Optical coherence tomography," *J. Biomed. Opt.*, vol. 1, no. 2, pp. 157–173, Apr. 1996.

[27] M. R. Hee, "Optical coherence tomography of the eye," M.S. thesis, Massachusetts Inst. Technol., Cambridge, MA, USA, 1997.

[28] A. F. Fercher, W. Drexler, C. K. Hitzenberger, and T. Lasser, "Optical coherence tomography - principles and applications," *Rep. Prog. Phys.*, vol. 66, no. 2, pp. 239–303, Jan. 2003.

[29] A. F. Fercher, C. K. Hitzenberger, M. Sticker, R. Zawadzki, B. Karamata, and T. Lasser, "Numerical dispersion compensation for partial coherence interferometry and optical coherence tomography," *Opt. Exp.*, vol. 9, no. 12, pp. 610–615, Dec. 2001.

[30] J. F. de Boer and T. E. Milner, "Review of polarization sensitive optical coherence tomography and stokes vector determination," *J. Biomed. Opt.*, vol. 7, no. 3, pp. 359–371, Jul. 2002.

[31] R. C. Jones, "A new calculus for the treatment of optical SystemsI. description and discussion of the calculus," *J. Opt. Soc. Amer.*, vol. 31, no. 7, pp. 488–493, Jul. 1941.

[32] D. Goldstein and D. H. Goldstein, *Polarized Light, Revised and Expanded*. Boca Raton, FL, USA: CRC Press, Jun. 2003.

[33] C. Zhang, B. Zhu, H. Zhu, W. Zeng, and W. Ren, "Novel polarization atmosphere michelson interferometer," *Opt. Eng.*, vol. 51, no. 10, Sep. 2012, Art. no. 101714.

[34] A. Beléndez, E. Fernández, J. Francés, and C. Neipp, "Birefringence of cellotape: Jones representation and experimental analysis," *Eur. J. Phys.*, vol. 31, no. 3, pp. 551–561, May 2010.

[35] H. Sata, M. Murayama, and S. Shimamoto, "5.4 properties and applications of cellulose triacetate film," *Macromol. Symp.*, vol. 208, no. 1, pp. 323–334, 2004.

[36] S. Iwata, H. Tsukahara, E. N. E. Nihei, and Y. K. Y. Koike, "Compensation for birefringence of oriented polymers by random copolymerization method," *Japanese J. Appl. Phys.*, vol. 35, no. 7R, Jul. 1996, Art. no. 3896.

[37] S. Nobukawa et al., "Birefringence and strain-induced crystallization of stretched cellulose acetate propionate films," *Polymer*, vol. 111, pp. 53–60, Feb. 2017.

[38] 3M, "3M product information sheet: Scotch magic tape 810," Oct. 2008. [Online]. Available: https://www.packbgr.com/images/3m-810.pdf

[39] H. Yamanaka, Y. Teramoto, and Y. Nishio, "Orientation and birefringence compensation of trunk and graft chains in drawn films of cellulose Acetate-graft-PMMA synthesized by ATRP," *Macromolecules*, vol. 46, no. 8, pp. 3074–3083, Apr. 2013.

[40] P. Velasquez, M. del Mar Sánchez-López, I. Moreno, D. Puerto, and F. Mateos, "Interference birefringent filters fabricated with low cost commercial polymers," *Amer. J. Phys.*, vol. 73, no. 4, pp. 357–361, Apr. 2005.

[41] A. Tagaya, S. Iwata, E. Kawanami, H. Tsukahara, and Y. Koike, "Anisotropic molecule dopant method for synthesizing a zero-birefringence polymer," *Japanese J. Appl. Phys.*, vol. 40, no. 10R, Oct. 2001, Art. no. 6117.

[42] M. E. A. Manaf, M. Tsuji, S. Nobukawa, and M. Yamaguchi, "Effect of moisture on the orientation birefringence of cellulose esters," *Polymers*, vol. 3, no. 2, pp. 955–966, Jun. 2011.

[43] P. Dias, A. Hiltner, E. Baer, J. Dun, H. Chen, and S. Chum, "Structure and properties of biaxially oriented polypropropylenes (BOPP)," in *Proc. Annu. Techn. Conf.*, 2006, vol. 5, pp. 2660–2664.

[44] C. A. Barrios, "Pressure sensitive adhesive tape: A versatile material platform for optical sensors," *Sensors*, vol. 20, no. 18, Jan. 2020, Art. no. 5303.

[45] H. Zappe, *Fundamentals of Micro-Optics*. Cambridge, U.K.: Cambridge Univ. Press, Sep. 2010.

[46] D. M. Kinyua, G. K. Rurimo, P. M. Karimi, S. N. Maina, and C. F. Ominde, "Interferometry analysis of cellophane birefringence," *Opt. Photon. J.*, vol. 3, no. 6, pp. 337–341, 2013.

[47] S. H. Yoo, R. Ossikovski, and E. Garcia-Caurel, "Experimental study of thickness dependence of polarization and depolarization properties of anisotropic turbid media using Mueller matrix polarimetry and differential decomposition," *Appl. Surf. Sci.*, vol. 421, pp. 870–877, Nov. 2017.

[48] A. A. Michelson, *Studies in Optics*. Chelmsford, MA, USA: Courier Corp., 1995.